Printability and Overall Cooling Performance of Additively Manufactured Holes With Inlet and Exit Rounding

Emma M. Veley[1]
Department of Mechanical Engineering,
The Pennsylvania State University,
State College, PA 16801
e-mail: emv53@psu.edu

Karen A. Thole
Department of Mechanical Engineering,
The Pennsylvania State University,
State College, PA 16801
e-mail: kthole@psu.edu

Michael T. Furgeson
Department of Mechanical Engineering,
University of Texas at Austin,
Austin, TX 78712
e-mail: mfurges@utexas.edu

David G. Bogard
Department of Mechanical Engineering,
University of Texas at Austin,
Austin, TX 78712
e-mail: dbogard@mail.utexas.edu

To improve cooling effectiveness of gas turbine hardware, various film cooling hole shapes have previously been researched. Unique design modifications have recently been made possible through the design freedom allotted by additive manufacturing (AM). As one example, creating a rounded inlet for a film-cooling hole can mitigate separation at the inlet. This study explores various geometric features by exploiting the uses of additive manufacturing for shaped film cooling holes at engine scale. Both printability and cooling performance were evaluated. Resulting from this study, additively manufactured holes with hole inlet and exit rounding were printed with some variations from the design intent (DI). The largest deviations from the design intent occurred from dross roughness features located on the leeward side of the hole inlet. The measured overall effectiveness indicated that an as-built inlet fillet decreased in-hole convection as well as decreased jet mixing compared to the as-built sharp inlet. Including an exit fillet, which prevented an overbuilt diffuser exit, was also found to decrease jet mixing. A particular insight gained from this study is the importance of the convective cooling within the hole to the overall cooling performance. In-hole roughness, which is a result of additive manufacturing, increased convective cooling within the holes but also increased jet mixing as the coolant exited the hole. The increased jet mixing caused low overall effectiveness downstream of injection.
[DOI: 10.1115/1.4056389]

Keyword: heat transfer and film cooling

Introduction

Increased thermal efficiencies in gas turbine engines are dependent upon high turbine inlet temperatures that require efficient cooling of the components. Film cooling, which is one example cooling method, uses compressor bleed air injected through the surfaces of turbine blades and vanes to create a cool film along turbine airfoils. The effectiveness of film cooling is dependent upon the shape of the hole as well as many other non-dimensional fluid parameters. Metal based additive manufacturing (AM) expands the design space for possible hole shapes beyond traditional manufacturing.

While complex cooling features can theoretically be printed using AM [1], current printing technologies have limitations. Compared to conventionally manufactured film cooling holes that use either laser drilling or electro-discharge machining (EDM), the sintering of powder layers in laser powdered bed fusion processes (referred to as additive manufacturing throughout this paper) generate high surface roughness levels that are inherent to the process. These roughness levels are challenging to post-process given the sizes of cooling holes and complexity of the supply channels.

Two examples of AM roughness features include partially sintered powder adhering to surfaces and dross features from unsupported overhanging surfaces. Multiple methods of altering the AM surface roughness result from component orientation [2,3] and tailoring the printing parameters [4–6]. Even with these methods, the surface roughness using state-of-the-art AM is beyond that of laser drilling or EDM methods. The inherent roughness and part warpage of AM also causes challenges in meeting tolerances of small features. There are challenges, too, in additively

manufacturing small circular channels depending upon diameter and build orientation [2,7]. All of these challenges are particularly important to achieve the goal of creating developmental turbine airfoils with additively manufactured film cooling holes. With these concerns, however, the overwhelming benefits of being capable of directly additively manufacture cooled turbine airfoils for quickly evaluating novel turbine cooling technologies are pushing the industry into further developing AM processes.

The research question for this study addresses the ability to additively manufacture specific features on engine scale film cooling holes with current AM capabilities and whether these features improve the overall cooling effectiveness. Four cooling hole shapes were printed involving two basic diffuser shapes with variations of fillet radii for the holes. These hole shapes were derived and previously reported by prior optimization studies [8].

Literature Review

For many years, shaped film cooling holes with lateral and forward expansion angles have been known to improve effectiveness compared to cylindrical holes [9,10]. Schroeder and Thole [11] introduced a public baseline shaped hole with 7 deg lateral and forward expansion angles, known as the 7-7-7 hole, that has provided a baseline geometry used by many researchers to understand important impacts on film cooling performance including: freestream turbulence intensity [12], internal and external cooling [13], in-hole roughness [14], additive manufacturing [15], and inlet rounding [16,17]. The 7-7-7 hole has been used as a baseline reference for comparison to other publicly available cooling holes [1] and was first additively manufactured at engine scales by Stimpson et al. [15].

For meter-diffuser shaped holes, Jones et al. [8] performed a computational optimization study with various expansion angles.

The computational results were validated through experimental measurements of adiabatic effectiveness with four hole shapes. From the more than 50 holes simulated in their study, the 15-15-1 (lateral and forward expansion angles) hole was found to have beneficial diffuser angles for improved adiabatic effectiveness. Their results indicated that the lateral expansion angle had a greater influence than the forward expansion angle on cooling performance. All of the cooling holes that were reported by Jones et al. [8] had rounded inlets, based on previous work of Jones et al. [16].

Rounding the inlets of film cooling holes has been shown to reduce the in-hole separation at the hole entrance that occurs due to a change in flow direction between the supply and the hole [18]. Fraas et al. [19] evaluated a shaped hole with a 10-10-10 diffuser and with a sharp inlet and a rounded inlet supplied by 90 deg cross-flow. The rounded inlets outperformed the sharp inlet in both adiabatic effectiveness and net heat flux reduction. Similarly, Jones et al. [16] also looked at a rounded and swept inlet for a 7-7-7 hole supplied by 90 deg cross-flow under varying channel and jet velocity ratios. The swept inlet, which is a turn of the hole inlet toward the coolant feed, had a negative impact on cooling as compared to the sharp inlet whereas the rounded inlet had similar performance to the sharp inlet at low channel velocities. At high coolant channel velocities, the swept and rounded inlet had higher effectiveness than the sharp inlet. Regardless of the inlet configuration, separation was still predicted to be present in the holes.

Hay et al. [20] studied the effects of rounding the inlet and the exit on the discharge coefficient of a cylindrical hole inclined at 30 deg. They found that although increasing the radii of the inlet fillet resulted in high discharge coefficients, changing the exit fillet had no effect on the discharge coefficient. Although a plethora of shaped holes studies exist [8,11–19], there is a lack of data on cooling effectiveness using fillets at the exit of meter-diffuser shaped holes.

Prior to studies appearing in the literature showing AM hole roughness impacts, Schroeder and Thole [14] used a controlled roughened surface in the metering and diffuser sections of 7-7-7 holes. Their results showed reduced adiabatic effectiveness levels when the roughness size exceeded the viscous sublayer especially at high blowing ratios. Within cooling holes, roughness inherent from the AM process has been shown to have a detrimental effect on the performance of film cooling [1,15].

Although surface roughness inside the film cooling hole has a negative impact on adiabatic effectiveness, the AM induced surface roughness increases the convective heat transfer within the film cooling hole, which is an important benefit of film cooling [21]. Stimpson et al. [15] printed 7-7-7 holes and compared the results to a smooth EDM hole. The EDM hole had a higher area-averaged overall effectiveness than the corresponding AM hole; however, the AM holes had significantly higher in-hole convection than the EDM holes due to the roughness features. Similar results were reported by Snyder and Thole [1] who additively manufactured publicly available cooling hole geometries. One of the key

results of their study showed that the printability of some hole features was not sufficient for the holes to operate as designed. Likewise, they saw that the small variations in the geometries from the AM process notably influenced the coolant coverage uniformity.

The present study provides an evaluation of the printability and cooling performance of as-built condition of a specific feature enhancement: rounding of film cooling hole inlets and exits. The uniqueness of this study was investigating additive manufacturing capabilities on engine scale cooling holes with these particular features and the combined influence of geometry and additive manufacturing defects on overall cooling effectiveness.

Geometric Description of Cooling Holes

Four test coupons, each with a different cooling hole shape, were printed to evaluate particular hole features on overall cooling effectiveness. The fifth coupon with no film cooling holes and the same internal channel aspect ratio was printed for the purpose of providing a cooling effectiveness reference without film cooling (ϕ_o).

Figure 1 shows the general definitions for the shape of the holes with the detailed geometric features listed in Table 1. All the holes in this study have shallow laidback angles (β_2) and wide lateral expansion angles (β_{lat}). The 9-9-3 diffuser also had a 2.2 deg angle on the windward side (β_1) tilting toward the metering axis. The naming convention of the hole geometry starts with the expansion angles (lateral and then forward) then the type of rounding, sharp inlet (SI), rounded inlet (RI), and rounded inlet and exit (RIE). For each hole the diffuser starts 2.5D from the hole inlet. Each hole had a total hole length of 6D.

To manufacture the five coupons, an EOS-M280 powder bed fusion machine was used with EOS Inconel 718 powder that had a diameter distribution of 20–55 μm [22] and layers of 40 μm. The machine parameters were standard and consistent between geometries. Each coupon had a row of five cooling holes spaced 6D apart. The axis of the hole metering section was oriented with the build direction (vertical) to produce the least amount of distortion from the design intent (DI) [3]. A combination of solid, hatched, and conical support structures was used to hold the parts to the substrate during the build process. The supports were removed after the build plate was annealed to remove stresses.

An industrial computed tomography (CT) scanner was used to nondestructively reconstruct a three-dimensional representation of each as-built hole. The scanning resolution for the holes was 20 μm (voxel size), and the software's adaptive surface determination ascertained the surface at one-tenth the voxel size (2 μm) [23]. Once the as-built surfaces of the coupons were deduced, these surfaces were directly compared to the design intent. Figure 2 shows cross sections of the design intent and the as-built surfaces. A cross-sectional slice along the streamwise direction at the center of the hole is shown for each hole, as well as two cross sections normal to the metering axis within the metering sections of the holes ($\ell/D = 1.9$ and 2.3).

The data in Fig. 2 indicate fairly good agreement between the as-built and the design intent surfaces; however, there are deviations derived from the AM resolution, which impacts the hole size, tolerancing on the expansion angles, and the fillets on inlets and exits. The minimum cross-sectional area of the cooling hole, which is also known as the metering area, is an important geometric parameter to quantify given it sets the cooling mass flowrate. Cross-sectional slices normal to the meter axis, such as those shown in Figs. 2 and 3, were used to calculate the cross-sectional areas and perimeters of the holes. The metering cross-sectional area for each film cooling hole occurs in the range of $1.74 < \ell/D < 2.28$ for all 20 holes.

Figure 3 shows the metering cross sections of all five holes in each coupon. Between the four coupons shown in Fig. 3, the 15-15-1 SI has the greatest variation in cross sections between the five holes including roughness features. The increased roughness in the 15-15-1 SI metering cross section can especially be seen on
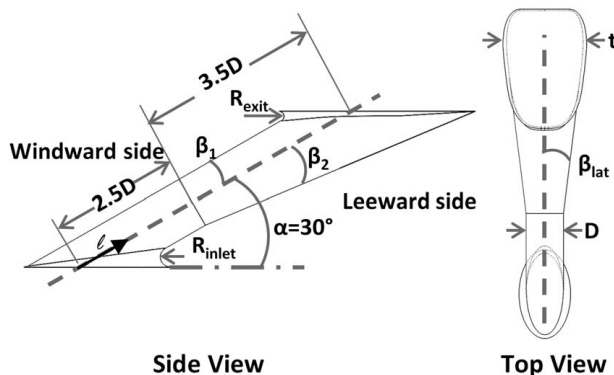

Fig. 1 Shaped hole with rounded inlet and exit

Table 1 Design intent of hole and coupon parameters

Hole shape	β_{lat}	β_1	β_2	R_{inlet}	R_{exit}	D (mm)	L_m/D	AR	P/D	t/P	t_{wall} (mm)	H/D
9-9-3 RI	8.6 deg	−2.2 deg	2.8 deg	0.25D	—	0.698	2.5	2.27	6	0.382	2.10	3.4
9-9-3 RIE	8.6 deg	−2.2 deg	2.8 deg	0.4D	0.2D	0.698	2.5	2.17	6	0.430	2.10	3.4
15-15-1 SI	15 deg	0 deg	1 deg	—	—	0.762	2.5	2.92	6	0.499	2.29	3.4
15-15-1 RI	15 deg	0 deg	1 deg	0.25D	—	0.762	2.5	2.79	6	0.499	2.29	3.4

the bottom of Fig. 3(c), which is the leeward side of the hole. The holes with inlet fillets, in general, are also rough on the leeward side of the inlet, as shown at $\ell/D = 1.9$ in Fig. 2. Because the fillet changes the diameter through the metering section of the hole, the filleted inlet holes have their metering cross section further into the hole. The 9-9-3 RI hole has the least variation of all the coupons between metering cross sections, with only the center hole having a significant deviation on the lower left side of the cross section as shown in Fig. 3(a). Both the 9-9-3 RIE in Fig. 3(b) and the 15-15-1 RI in Fig. 3(d) have similar variations between holes.

Table 2 highlights the average as-built diameter and minimum cross-sectional areas of each design normalized by the design intent reported in Table 1. All of the holes had hydraulic diameters

and metering areas that were larger than the design intent, which are also shown in Fig. 2. Similarly, Snyder et al. [1] also saw cross-sectional areas in AM as-built film cooling holes that were larger than the corresponding design intent. According to Wildgoose et al. [2], vertically built cylindrical microchannels can be expected to have mean hydraulic diameters at least 5% greater than the design intent. The variation in the metering cross-sectional area given in Table 2 is consistent with what is shown in Fig. 3. Although the 9-9-3 RI average metering cross-sectional area has the highest deviation from the design intent, it has the least variation between holes of all four coupons. Conversely, the 15-15-1 SI has the average cross-sectional area nearest to the design intent, but also has the highest deviation between holes of all four coupons. The high deviation in the minimum cross-sectional area of the 15-15-1 SI holes is attributed to the surface roughness at these locations, shown in Fig. 3(c).

To better understand the high roughness on the leeward side of the hole inlets, the outlines in Fig. 2 can be examined. For the $\ell/D < 1.9$ locations, the views perpendicular to the flow direction in Fig. 2 show large features deviating from the design intent on the leeward side. The greatest deviation from the design intent occurs for the 9-9-3 RIE hole, shown in Fig. 2(b), due to the dross roughness on the leeward side of the inlets. During the AM process, because the metering axis was perpendicular to the substrate, the coolant feed channel was oriented at 60 deg to the
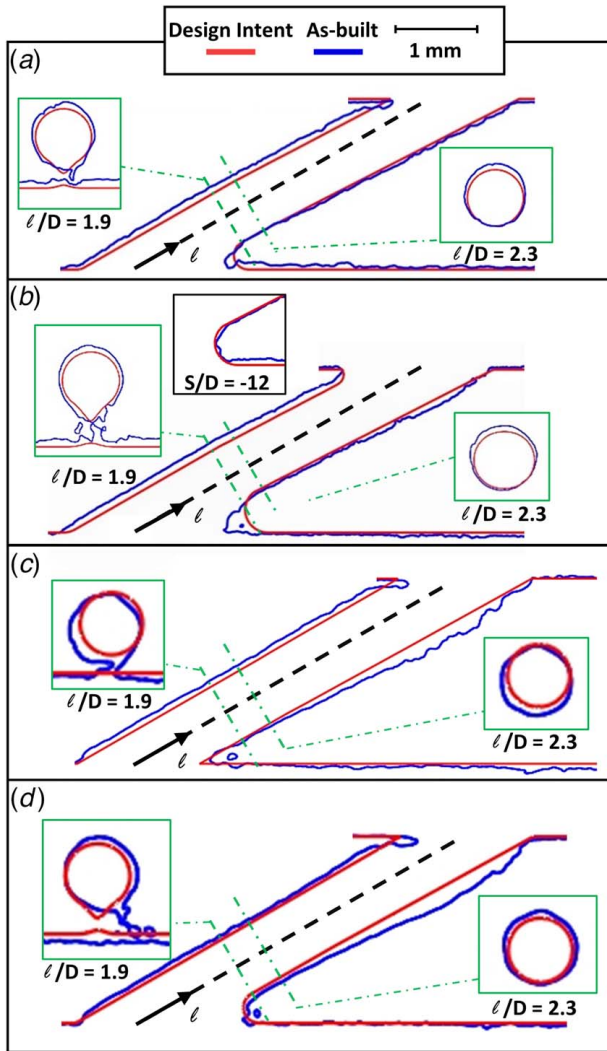

Fig. 2 Cross sections of CT scanned as-built (blue) and best-fit design intent (red) of the (a) 9-9-3 RI, (b) 9-9-3 RIE, (c) 15-15-1 SI, and (d) 15-15-1 RI holes
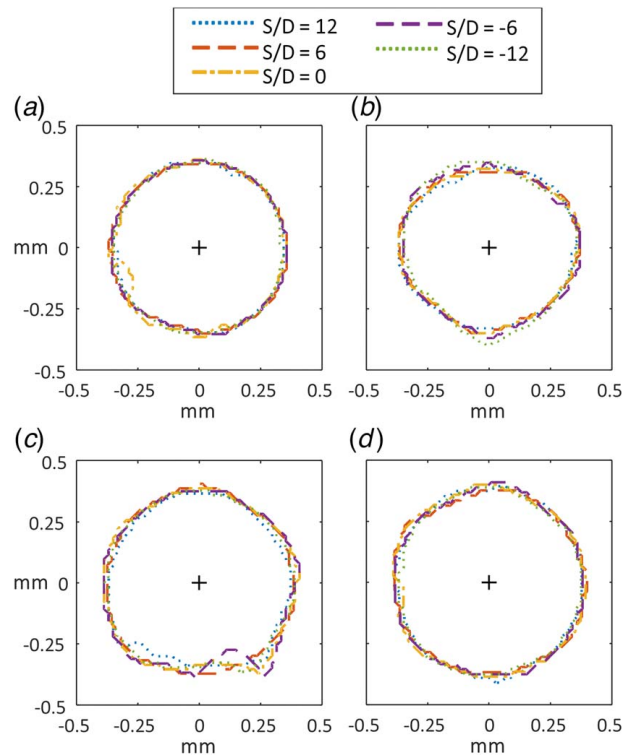

Fig. 3 Cross sections of (a) the 9-9-3 RI hole, (b) the 9-9-3 RIE hole, (c) the 15-15-1 SI hole, and (d) the 15-15-1 RI hole with the minimum cross-sectional area

Table 2 As-built hole parameters

Hole	$\dfrac{D}{D_{DI}}$	$\dfrac{A_{c,min}}{A_{c,min,DI}}$	$\dfrac{t_{wall}}{t_{wall,DI}}$	R_a (μm)	$\dfrac{R_a}{D}$
9-9-3 RI	1.09 ± 0.04	1.21 ± 0.01	0.987	6.5	0.0085
9-9-3 RIE	1.04 ± 0.05	1.13 ± 0.02	0.968	12.7	0.017
15-15-1 SI	1.004 ± 0.02	1.05 ± 0.04	0.997	11.7	0.015
15-15-1 RI	1.05 ± 0.04	1.08 ± 0.02	0.983	10.5	0.013

substrate. In this orientation, the leeward sides of the cooling hole inlets are built as arches over unsintered powder. Increasing the inlet fillet radius increases the arch distance, which in turn produces a large region for dross features to form. The 9-9-3 RIE holes had the largest arch distance and the largest dross features size present on four of the five holes. The fifth hole, located at S/D = −12 and shown in Fig. 2(b), does not have a large dross feature and is consequently the 9-9-3 RIE hole closest to the design intent. The lack of a large dross feature on only one of the 9-9-3 RIE hole is the largest variation between holes in any of the coupons. The design with the smallest dross features was the 15-15-1 SI, shown in Fig. 2(c), which was designed with no inlet fillet and the smallest distance to bridge. The holes with 0.25D inlet fillets had similar dross feature sizes.

Another common deviation between holes that is evident in Fig. 2 is the overbuilt lip on the windward side of all the diffusers except the 9-9-3 RIE hole. The holes with standard exits on the diffuser are designed to where the thickness of the windward exit wall is less than that of a melt pool. Therefore, during printing the melt pool caused the surface to overbuild.

Local deviation contours from the design intent are shown in Fig. 4, using a single hole to represent each geometry. The CT scans were fitted to the design intent model using a best-fit based upon geometric features. Positive values of deviation indicate material was present where there was no intended material in the design. Negative values indicate material was not present where there was intended material in the design.

For all of the holes, the view at the inlets in Figs. 4(a)–4(d) shows dross roughness features on the leeward side of the inlets. Also indicated for all the holes is partially sintered powder along the channel walls as well as in the diffuser as indicated in Figs. 4(e)–4(h). As was already mentioned, there are significant dross features on the leeward side of the hole inlets due to the unsupported material during the build. Both the depth and width of the melt pool cause the intended sharp inlet of the 15-15-1 SI design to become rounded, as shown in Fig. 4(c). This natural rounding creates a small fillet on the leeward side of the inlet; however, the fillet is
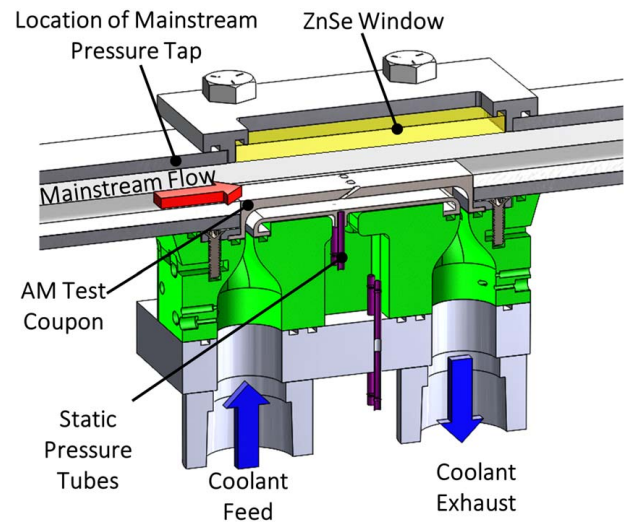
Fig. 5 Cutaway view of rig test section used to measure the overall effectiveness of film cooling in AM coupons

still smaller than the fillets designed into the other holes as was also indicated in Fig. 2.

The contours for the two 15-15-1 holes (Figs. 4(c), 4(d), and 4(h)) indicate that the channels walls were much closer to the design intent than the 9-9-3 holes that have high negative deviation contours on the internal walls. The thickness of the wall separating the coolant and the mainstream, t_{wall}, relates to the conduction through the wall which affects overall cooling effectiveness. The average wall thicknesses of all coupons were within 4% of their design intent. The as-built t_{wall} values are reported in Table 2, with a standard deviation of 13 μm. Given that the thermal resistance for conduction through the wall was approximately 7% of the total thermal resistance, the 9% difference in wall thickness between the 9-9-3 and the 15-15-1 coupons had insignificant effects on the overall cooling performance parameter.

The surfaces in Fig. 4 also show the roughness due to the partially sintered power in the metering and diffuser sections of the holes. Given the size of the film cooling holes at engine scale, AM roughness features create blockages. To quantify the surface roughness in the holes, the arithmetic mean roughness, R_a, which is a measure of the average distance of the surface from a mean fitted surface, was calculated from the CT scan surfaces. A plane was fitted, using a Gaussian distribution, to the laidback surface of the diffuser of each hole. The resulting average R_a, listed in Table 2, of 9-9-3 RI
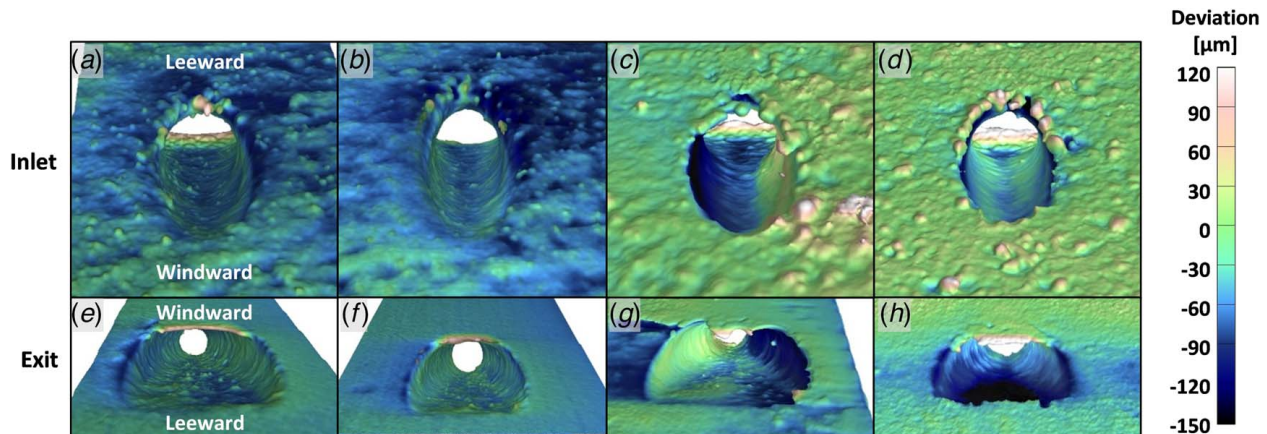

Fig. 4 Local deviations from the best-fit design intent of a single hole from each geometry: (a), (e) 9-9-3 RI, (b), (f) 9-9-3 RIE, (c), (g) 15-15-1 SI, and (d), (h) 15-15-1 RI. The view of the inlets (a)–(d) shows the dross roughness features.

Table 3 Rig operating conditions

Parameter	Coolant	Mainstream
Mach number	<0.1	0.3
Upstream $Re_{i,u}$	Varied for M, D_h	
Downstream $Re_{i,d}$	14,000	
$Re_{D_{h,\infty}}$		220,000
Film cooling DR	1.23	
Bi	0.2	

is approximately half that of 9-9-3 RIE, which has a similar roughness to both 15-15-1 holes.

Experimental Approach

This study used an experimental rig, shown in Fig. 5, similar to that used by Stimpson et al. [15] and Snyder et al. [1] to obtain the overall effectiveness of the as-built hole geometries at engine relevant conditions. The experimental rig was designed and instrumented to measure various temperatures and pressures, which were used for the calculation of effectiveness and mass flowrates. The AM coupon was installed between a set of plenums, where coolant flow passed through the feed channel in the AM coupon. Mainstream air passed over the top outer surface of the coupon. The mainstream channel had a height of about 13 cooling hole metering diameters with an aspect ratio of $W/H = 2.7$ (25.4 mm × 9.5 mm). The hydraulic diameter of the mainstream channel was 13.8 mm with an approach length of 38 times the channel hydraulic diameter prior to reaching the test coupon, thereby ensuring hydraulically fully developed flow at the film cooling holes. A single cooling channel inside the AM coupon fed the row of holes having an approach length of 4.1 times the hydraulic diameter of the coolant channel, a channel height of 3.4 cooling hole diameters (D), and a channel aspect ratio of $W/H = 8.1$.

Pressure regulators upstream of the test section in both the mainstream and the coolant supply were used in conjunction with downstream valve to set the three defining flowrates: Ma_∞, M, and Re_i. Note for this particular test rig, the Mach and Reynolds numbers can be controlled independently by setting the downstream pressure. A turbine flowmeter measured the mainstream flow entering the test section. A laminar flow element measured the coolant exhaust mass flowrate. The external flow over the coupon was heated air at a nominal temperature and pressure of 60 °C and 360 kPa respectively. The coolant was gaseous nitrogen at −5 °C. The pressure in the coolant channel varied with blowing ratio, while the downstream internal Reynolds number ($Re_{i,d}$) remained constant for all blowing ratios.

A ZnSe window with a transmissivity of 0.7 was installed on the top wall of the mainstream channel, as shown in Fig. 5. The AM test coupons were painted black to provide an emissivity of 0.97. An infrared (IR) camera was positioned above the window at an angle to reduce reflections of the camera itself. The region around the camera and window was covered with a black containment unit to mitigate reflections of the surroundings. Three surface mounted thermocouples on the coupon were used to calibrate the IR images, which allowed for accurate measurements of the surface temperature. Of the five holes in the coupon, the camera viewed the full pitches of the center three holes. The small portion of the outer two holes that were visible was not considered during analysis to eliminate any averaging bias or edge effects.

Several operating conditions used in the overall cooling effectiveness experiments were set to match turbine conditions: density ratio (DR), downstream internal channel Reynolds number ($Re_{i,d}$), and blowing ratio (M). The density ratio and the internal Reynolds number downstream of the cooling hole were both held constant as listed in Table 3. The density ratio was matched by using cold gaseous nitrogen (N_2) as the coolant flow

for a constant DR = 1.23. The channel Reynolds number downstream of the cooling holes was held constant to maintain the same downstream boundary condition by adjusting the upstream mass flow to account for the flow exiting the cooling holes. Except when specifically noted, the Mach number of the mainstream was held at $Ma_\infty = 0.3$ while the coolant supply channel Mach number remained incompressible ($Ma_i < 0.1$). The blowing ratio was varied from $0.6 < M < 3$. The centerline velocity for the mainstream channel was calculated assuming the one-seventh velocity profile and was related to the average mainstream velocity by a ratio given by Kay et al. [24] of $V/U_\infty = 0.81$. The Biot number was held constant at an engine relevant Biot number.

For the film cooling experiments reported in the results section, the coolant temperature, T_c, at the inlet of the film cooling holes (rather than the inlet to the cooling channel) was used to define the overall effectiveness measurements as well as the blowing ratios. Since the temperature at the inlet of the film cooling holes was not directly measured, it was estimated based upon separate experiments conducted using the fifth coupon with no film cooling holes to estimate the internal convection coefficient, h_i. Assuming the walls of the coolant channel were isothermal and by measuring the external surface temperature as well as the inlet and exit temperatures of the coolant channel, a one-dimensional (1D) heat transfer analysis was performed on the data from the coupon with no cooling holes to estimate h_i for a range of Re_i.

The estimated h_i from the coupon with no film cooling holes was then used to calculate the temperature at the inlet of the film cooling holes in the other four coupons. Using the estimated h_i for $Re_{i,u}$ and the measured inlet temperature to the supply channel, further 1D conduction analyses were performed to calculate T_c at the inlet to the film cooling holes. The coolant temperature was verified through an additional 1D conduction analysis using the estimated h_i for $Re_{i,d}$ and the calculated T_c to calculate the temperature at the exit of the coolant channel, which was also measured with thermocouples. The calculated exhaust temperatures were always within 1 °C of the measured coolant exhaust temperatures.

The uncertainty of several parameters was calculated using the propagation of uncertainty described in Figliola and Beasley [25]. The uncertainty in DR is dependent only upon the temperature and has a low uncertainty of 2%. The uncertainty of M is dependent upon temperature, the pressures, and the geometric parameters, and has an uncertainty of 10%. The uncertainty of M is driven by the uncertainty in the metering cross-sectional area, which is a function of the voxel size and the area. For the area-averaged overall effectiveness measurements, an average of ten IR images was used to reduce the precision uncertainty. The uncertainty in effectiveness was ± 0.017 at the lowest tested blowing ratio ($M = 0.6$) and ± 0.016 at the highest tested blowing ratio ($M = 3.0$), with the uncertainty driven by the uncertainty in the IR images. Based on three
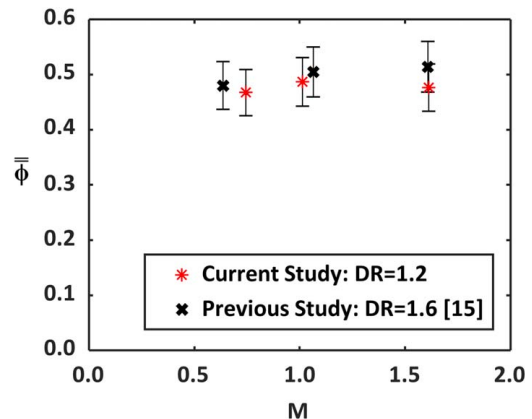

Fig. 6 Area-averaged overall cooling effectiveness ($0 \leq X/D \leq 20$) of the 7-7-7 EDM hole at two different density ratios
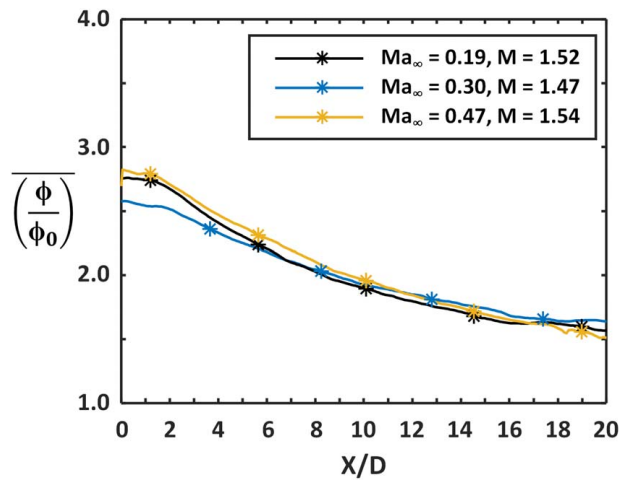
Fig. 7 Lateral averages of the augmentation in effectiveness of the 15-15-1 RI at *M* = 1.5 for three Mach numbers
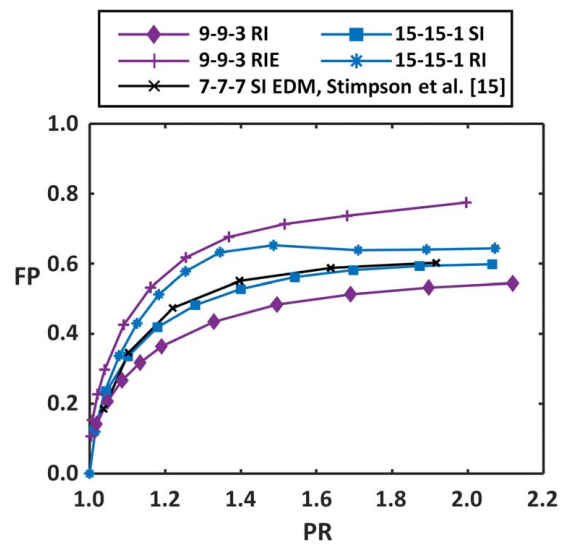

Fig. 8 The flow parameter as a function of pressure ratio which is used to calculate the mass flowrate through the holes at a given PR, the EDM 7-7-7 from Stimpson et al. [15] is included for reference.

independent tests, the repeatability in augmentation of effectiveness was within 5%.

Using a test coupon with EDM 7-7-7 holes previously used by Stimpson et al. [15], a benchmarking test was completed to compare with their published data. These comparisons are made in Fig. 6 for the area-averaged overall effectiveness for several blowing ratios. The overall effectiveness was within 10% between the original and current experiments, which was within the stated uncertainty.

Determining the effect of Mach number is important in considering the hole placement on a turbine blade given the variations along the surface. Previous studies have shown minimal effect on cooling effectiveness at low blowing ratios subjected to subsonic external flows [10,26]. To verify the compressibility effect is also negligible with rough holes, an investigation was conducted using three Ma_∞ cases: $Ma_\infty = 0.19, 0.30$, and 0.46. The back pressure in the rig was varied using a throttling valve to obtain the three Ma_∞ while maintaining the Reynolds number of the mainstream of $Re_\infty = 220,000$, downstream internal channel $Re_i = 14,000$, and the blowing ratio at 1.5. Only the 15-15-1 hole with a rounded inlet was tested for the compressibility tests.

The lateral average augmentations in effectiveness at the three Ma_∞ are shown in Fig. 7. Minimal variation between the different cases indicated that the operating Mach number had no significant effect on the cooling performance, which is consistent with previous studies [10,25]. Because of the negligible impact of Mach number, comparisons between studies with operating Mach numbers in the compressible regime can be made to large-scale incompressible experiments.

Setting Film Cooling Flowrates

Flowrates through the film cooling holes were set using a pressure ratio (PR) and flow parameter (FP) curve that was attained through separate experiments. These separate experiments were conducted by closing the coolant exhaust and simultaneously measuring the mass flowrate of supplied air through the cooling holes using a mass flowmeter and measuring the PR. The mass flowrate was converted to the non-dimensionalized FP which compensates for variations in gas type, pressure, and temperature between the flow tests and the effectiveness tests.

After knowing the flow parameter as a function of pressure ratio for a particular hole geometry, the internal and external pressures are measured and set to achieve the desired cooling flowrates. The cutaway view of the test section in Fig. 5 shows static pressure taps in the feed channel at the inlet of the cooling holes along with the location static pressure was measured in the mainstream to calculate the pressure ratio across the cooling holes.

The results of the measured flow parameters as a function of pressure ratio for each of the holes are shown in Fig. 8. For a given PR, the flow parameters for the 9-9-3 RIE and the 15-15-1 RI were higher than for a baseline 7-7-7 cooling hole coupons in which the holes were made using EDM [15] (rather than printing the holes through AM). The increase in flow parameter for a given pressure ratio that was present for the 9-9-3 and 15-15-1 holes is a result of the expanded hole exit that acts as a diffuser. The literature indicates that holes with larger area ratios (ARs) typically have higher discharge coefficients relative to small area ratios for a given pressure ratio [1,10], but the discharge coefficients are also dependent upon the inlet rounding [20].

Rounded inlets for cylindrical film cooling holes have been reported to provide an increased flowrate compared with sharp inlets at the same pressure ratio [20]. The results in Fig. 8 indicate higher flow parameters for the same pressure ratios for the 15-15-1 holes with a rounded inlet compared with the sharp inlet. Figure 8 also shows that the 9-9-3 RIE hole has an FP value that is as much as 50% higher than the 9-9-3 RI hole. This difference in FP can be partially attributed to the larger inlet radius for the 9-9-3 RIE compared with the 9-9-3 RI (see Table 1). However, the rounded exit of the 9-9-3 RIE hole may also be a significant factor. As indicated in Fig. 2, and discussed previously, the 9-9-3 RIE hole did not have an upstream lip partially covering the exit of the hole, while the 9-9-3 hole did have this lip, which probably decreases the FP parameter. From the results shown in Fig. 8, the 9-9-3 RI has a lower flow parameter than the 15-15-1 SI, which is likely due to a larger area ratio for the 15-15-1 SI hole, regardless of the inlet rounding. Comparing the flow parameters of the 9-9-3 RIE and the 15-15-1 RI is of particular interest since the AR for the 9-9-3 hole is smaller relative to the AR of the 15-15-1 hole. There are two compounding causes for the larger 9-9-3 RIE FP compared to the 15-15-1 RI FP. The first cause is a result of the larger rounding radius of $0.4D$ for the 9-9-3 RIE inlet fillet compared to the $0.25D$ of the 15-15-1 RI inlet fillet. The second cause is the presence of an overbuilt lip on the diffuser exit of the 15-15-1 RI hole (shown in Fig. 2(*d*)), which has an adverse effect on the flow passing through the 15-15-1 RI.

Computational Approach

Reynolds-averaged Navier–Stokes simulations were performed for a smooth wall 9-9-3 RI hole using ANSYS FLUENT 2020R1. The
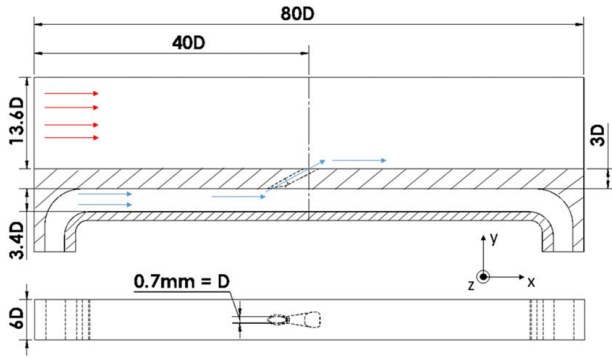
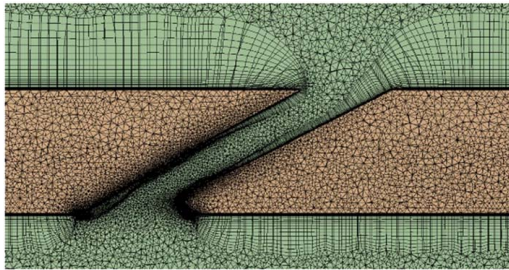**Fig. 9 Computational domain used to model flow in the described test section**

Fig. 10 Hole midplane documenting the near-hole mesh

computational domain used in this study, shown in Fig. 9, was representative of the experimental facility. Both solid and fluid bodies were included to facilitate conjugate heat transfer computations. A single hole was used in the simulation, but a periodic condition was used at the domain edges in the lateral or z-direction, so that a row of holes was simulated.

The near-hole mesh used in this study is presented in Fig. 10. The entire mesh was developed in ANSYS Mechanical 2020 and was constructed with tetrahedrons for simplicity. The global element size was set to 0.25D. In the regions encapsulating the film cooling hole and film jet, boundaries of influence were applied with finer resolution.

Inflation layers were applied to the walls. These inflation layers properly resolve the boundary layer. For this mesh, three inflation layers were defined: One for the rounded inlet of the film cooling hole, one for the metering section and diffuser section of the film cooling hole, and one for every other wall surface (global). For all inflation layers, the first layer height was $y^+ \approx 1$.

Grid independence for this mesh was established by performing a prediction of the same $M = 2$ case using three different grid sizes:

Table 4 Simulation boundary conditions

Location	Type	Value	Units
Coolant inlet	Mass flow	Varies[a]	g/s
Coolant inlet	Temperature	258–264	K
Coolant inlet	Turb. intensity	5	%
Coolant inlet	Length scale Λ/D	1	(—)
Coolant inlet	Mass flow	0.49	g/s
Mainstream inlet	Velocity	Profile[a]	m/s
Mainstream inlet	Temperature	333	K
Mainstream inlet	Imported k	Profile[a]	m²/s²
Mainstream inlet	Imported ε	Profile[a]	m²/s³
Mainstream inlet	Pressure	3.6	bar

[a]See text

3.7 million elements, 6.8 million elements, and 12.5 million elements. Taking the area-averaged overall cooling effectiveness over a range of $X/D = 5$ to 30, there was a maximum 0.5% variation in $\overline{\overline{\phi}}$ between the 6.8 million cell case and 12.5 million cell case; therefore, the 12.5 million element mesh was used.

The realizable $k - \varepsilon$ turbulence model (RKE) with enhanced wall treatment was used in this study. In comparison to other models, Harrison and Bogard [27] found the RKE model best predicted both centerline effectiveness and heat transfer augmentation when compared to experimental data. Jones et al. [16] found that the RKE model was best at predicting coolant distribution at the outlet of the hole. The pressure-based solver was used. Second-order upwind spatial discretization paired with a least squares cell-based gradient was implemented.

Boundary conditions are summarized in Table 4. In the mainstream, a uniform pressure outlet and fully developed $Ma_\infty = 0.3$ velocity profile inlet were applied. The turbulent parameters k and ε were imported from the fully developed profile. At the inlet and outlet of the coolant channel, mass flowrate conditions were specified, which set the film cooling blowing ratio. The downstream mass flowrate was fixed to match $Re_i = 14,000$. For the internal coolant channel nominal turbulence conditions of $\Lambda/D = 1$ and $TI = 5\%$ were applied. Mainstream and coolant temperatures were defined for a density ratio of $DR = 1.26–1.29$, matching the experimental conditions. The fluid domain for the mainstream and coolant was modeled as air, and the solid domain was modeled as Inconel 718 with a thermal conductivity of 9.77 W/m · K. Although gaseous nitrogen was used as coolant in the experiments, air was used in the simulation for simplification. The simplification should have negligible impact on the heat transfer calculations due to the similar gas properties of nitrogen and air.

Overall Cooling Effectiveness

The overall effectiveness for film-cooling is dependent upon three convective heat transfer mechanisms: supply channel convection, in-hole convection, and external film cooling. For all four hole shapes, the downstream internal Reynolds number ($Re_{i,d}$) was held constant to provide the same supply channel convection. While maintaining $Re_{i,d}$, the upstream internal Reynolds number ($Re_{i,u}$) varied depending upon hole diameter to achieve various blowing ratios. The data reported in this section are in terms of an augmentation in cooling effectiveness (ϕ/ϕ_0) where ϕ_0 is the local cooling effectiveness measured with no film-cooling. As such, the results presented provide the benefit of film cooling relative to a non-film-cooled surface.

Figure 11 shows contours of the local augmentation of overall effectiveness for all four hole shapes at three blowing ratios ($M = 1.5$, 2, and 3). Immediately evident from Fig. 11 is that the cooling uniformity for the 15-15-1 holes is more two-dimensional (more uniform coverage) than the 9-9-3 holes. Also apparent is that the augmentation in effectiveness increases with blowing ratios regardless of cooling hole shape. For both the 9-9-3 RI and the 9-9-3 RIE there are noticeable variations in effectiveness between the different holes for the same geometry, as shown in Figs. 11(a) and 11(b), which can be attributed to manufacturing variations from AM. Lateral averages ($\overline{\phi/\phi_0}$) of the center three holes at $M = 1.5$ are shown in Fig. 12 to show the variability due to the AM build. The 9-9-3 holes (Fig. 12(a)) show greater variation in lateral averages between holes than the 15-15-1 holes (Fig. 12(b)). However, even with the variability between holes in a coupon, unique trends between coupons can be seen in Fig. 12. For example, all 9-9-3 RIE holes have a low rate of decay in the streamwise direction and therefore have higher downstream ($X/D > 10$) effectiveness compared to the 9-9-3 RI holes.

Examining the contours of the 9-9-3 RI and 9-9-3 RIE in Fig. 11, the cooling effectiveness immediately downstream of the diffusers is similar between the 9-9-3 RI and the 9-9-3 RIE. However, the 15-15-1 SI has higher effectiveness levels just downstream of the
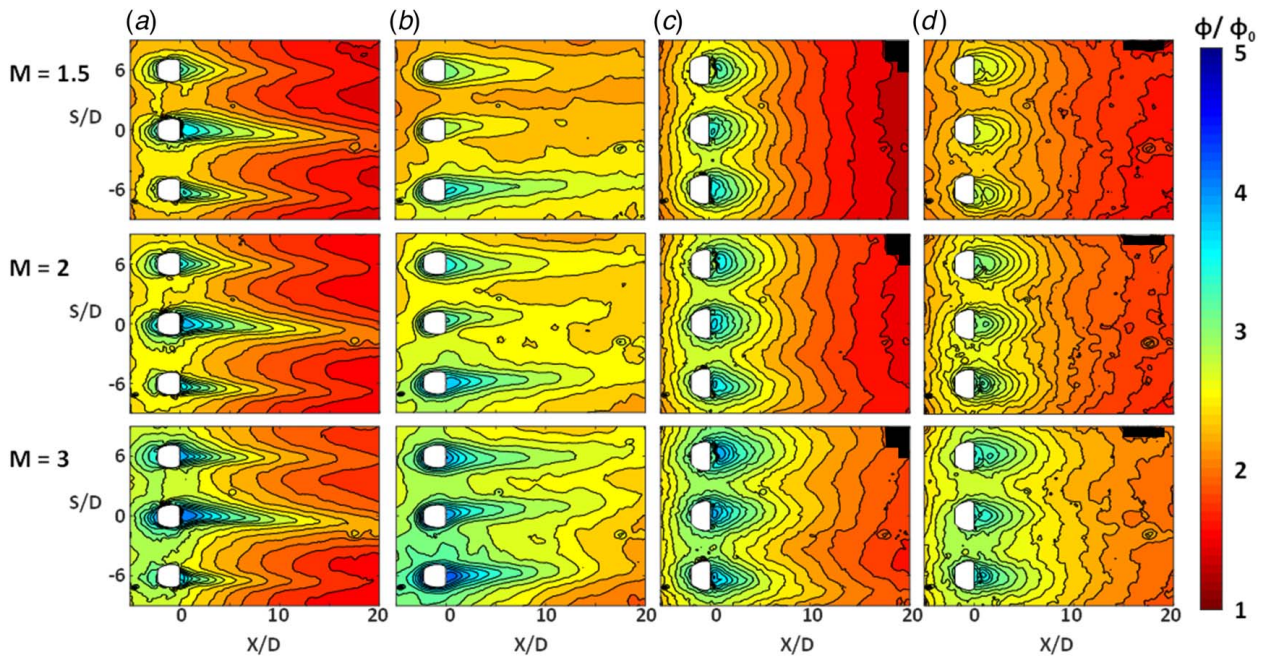
Fig. 11 Contours of the augmentation in cooling effectiveness at *M* = 1.5, 2.0, and 3.0 for the (*a*) 9-9-3 RI, (*b*) 9-9-3 RIE, (*c*) 15-15-1 SI, and (*d*) 15-15-1 RI. Black regions are the location of surface thermocouples and were not included in averages.

cooling holes as compared with the 15-15-1 RI for all blowing ratios.

The trends in augmentation of effectiveness are also evident in the lateral averages across the center three holes shown in Fig. 13. At $M = 1.5$ (Fig. 13(*a*)), the 15-15-1 SI hole gave the highest effectiveness of all four holes in the near-hole region. The 15-15-1 RI had a much lower cooling immediately downstream of the diffuser than the 15-15-1 SI; however, at $X/D \geq 9$, the 15-15-1 RI had a higher lateral average than the 15-15-1 SI. In contrast, the 9-9-3 RI and RIE had nearly the same performance at the hole exit but the 9-9-3 RIE had a much lower decay and resulted in much better cooling along the $X/D > 0$ surface as compared with the 9-9-3 RI geometry. When comparing the decay rate in the streamwise direction between hole designs, slow decay rates indicate reduced film mixing. Reduced mixing with the mainstream results in high downstream effectiveness.

At the highest blowing ratio, $M = 3$, the laterally averaged effectiveness levels in Fig. 13(*b*) show a noticeably higher overall cooling effectiveness for the 9-9-3 RIE compared with the 9-9-3 RI cooling holes. For the high blowing ratio, $M = 3$, a similar slow decay resulted for the 9-9-3 RIE compared with the other three holes. The two 15-15-1 holes have similar lateral averages at $M = 3$.

The objective of rounding the inlet of shaped film cooling holes is to mitigate flow separation at the hole inlet. Reducing separation at the inlet decreases the non-uniformity of the cooling flow exiting the hole, which can lead to reduced mixing [16,17,19]; however, as the comparison of 15-15-1 SI to the 15-15-1 RI showed, the increase in the inlet fillet radius resulted in a decrease of augmentation in effectiveness immediately downstream of the diffuser (Figs. 13(*a*) and 13(*b*)). And as was previously stated, the decay rate of the effectiveness has a greater dependency on the exit fillet than the inlet fillet. The reduction in overall effectiveness from the sharp inlet to the rounded inlet may be caused by AM roughness deviations.

Near-Hole Convection Effects

The variations between the contours in the region upstream of the cooling holes, which is driven by in-hole convection, are a strong function of the diffuser shape and the inlet fillet radius, as shown in Fig. 11.

The windward start of the hole inlet is at $X/D \approx -7.8$, with some variation between holes due to fillet radii. The contours upstream of the diffuser trailing edge ($-5 \leq X/D \leq 0$) in Fig. 11 show that as blowing ratio increases, the near-hole overall effectiveness increases for each hole. Comparing the lateral averaged augmentation in effectiveness upstream of the diffuser exits, as shown in Fig. 13, the 9-9-3 diffusers tend to have similar or higher near-hole augmentations in effectiveness than the 15-15-1 holes at both $M = 1.5$ and $M = 3.0$ because of the small aspect ratio of the 9-9-3 hole. Inlet fillets also affect the in-hole convection. Because rounded inlets promote a decrease in separation, the maximum velocity decreases for holes with inlet fillets. Low local velocities have low local convection. Although the 9-9-3 holes have higher lateral averages upstream of the diffuser exit, the 15-15-1 holes have higher near-hole augmentations in effectiveness than the 9-9-3 holes, as shown in Fig. 11. The higher coverage ratio of the 15-15-1 holes, see Table 1, is presumably the cause of the better cooling between the 15-15-1 holes than the 9-9-3.

The near-hole, area-averaged augmentation in cooling effectiveness, shown in Fig. 14, was averaged between $-5 \leq X/D \leq 0$ with the region within the holes removed from the average. Starting the average at $X/D = -5$ keeps the averaging area consistent over a region with $Re_i = 14k$ regardless of the inlet fillet size given the location of the hole inlet.

Figure 14 shows that for all blowing ratios, the 15-15-1 SI hole had a higher near-hole effectiveness than the 15-15-1 RI. The fillet on the rounded inlet increased the inlet cross section area is expected to decrease the separation region in the inlet of the hole and thereby decreased the mean velocity compared to the sharp inlet hole. This would be expected to decrease internal bore cooling and hence decrease overall cooling effectiveness in the near-hole region. The 9-9-3 holes had very similar near-hole area averages. Overall, the differences between the near-hole augmentation of effectiveness for the four holes decrease at high blowing ratios. The decrease in spread indicated that there is a tradeoff between hole geometry and cooling flowrates for the near-hole effectiveness.
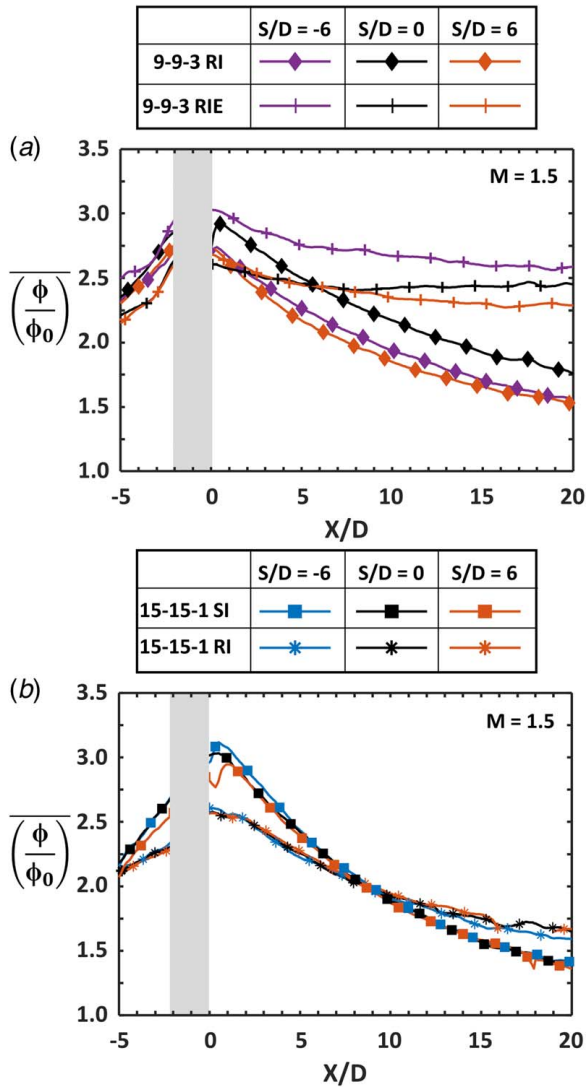
Fig. 12 Lateral averages of augmentation in cooling effectiveness at $M = 1.5$ of the center three holes in (a) the 9-9-3 coupons and (b) the 15-15-1 coupons

Fig. 13 Lateral averages over the pitches of the center three holes ($-9 \leq S/D \leq 9$) of the augmentation in cooling effectiveness at (a) $M = 1.5$ and (b) $M = 3$

Overall Benefit From Film Cooling

The area-averaged augmentation in effectiveness ($\overline{\overline{\phi}}/\overline{\overline{\phi}}_0$) over a range of blowing ratios is shown in Fig. 15(a) for different blowing ratios. Comparing holes, the 9-9-3 RIE hole, which was the only hole with an exit fillet, had the best overall cooling performance, as shown in Fig. 15(a). The other three holes have very similar $\overline{\overline{\phi}}/\overline{\overline{\phi}}_0$ across the blowing ratios investigated. Recall that the lateral averages of the 9-9-3 RIE hole, shown in Fig. 13, had reduced decay in the streamwise direction which indicated less film mixing than the other holes.

Because turbine engines run by setting a pressure ratio instead of a blowing ratio, it is important to understand the hole performance not only as a function of blowing ratio but also as a function of pressure ratio. Figure 15(b) shows the area-average augmentation in effectiveness across a range of pressure ratios. Although the 15-15-1 holes appeared to have similar area-averaged augmentation in cooling effectiveness when examined over a range of blowing ratios, the 15-15-1 RI has a better area-average cooling effectiveness when compared in terms of pressure ratio as shown in Fig. 15(b). Similarly, the 9-9-3 RIE requires a lower pressure ratio than the 9-9-3 RI to obtain the same blowing ratios. Interestingly, the 9-9-3 RI and the 15-15-1 SI have similar area-averages
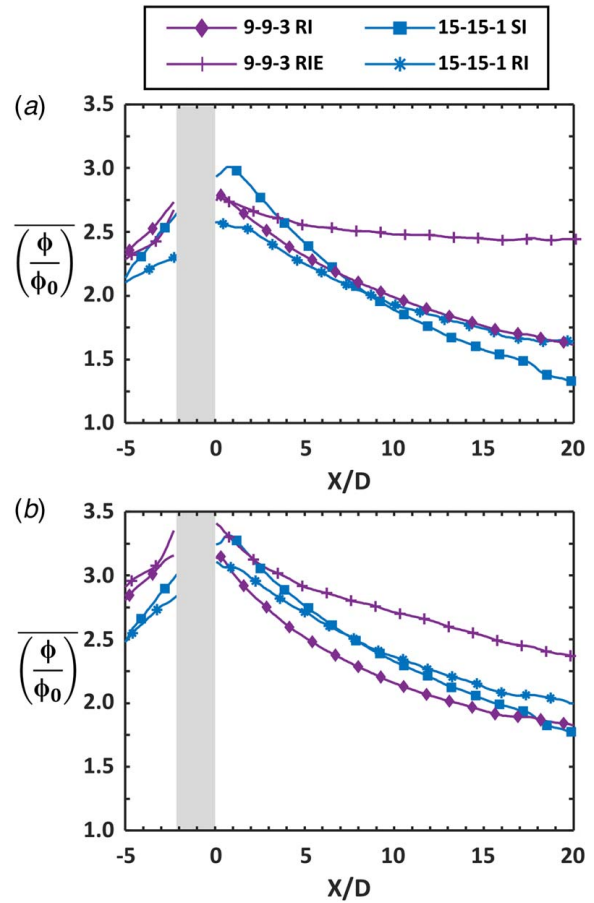
for the same pressure ratios. As seen from the lateral averages in Fig. 13, the as-built rounded inlets tend to decrease film mixing, but the 15 deg lateral expansion angle increases lateral spreading. The tradeoff between the film mixing and the lateral expansion caused the 9-9-3 RI and the 15-15-1 SI to have similar area-averaged augmentation in cooling effectiveness across pressure ratios.
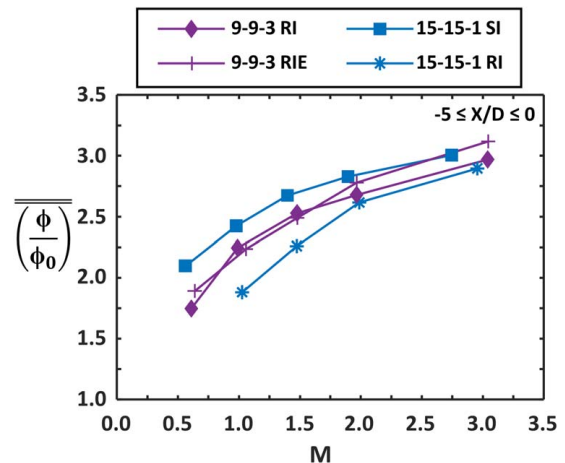

Fig. 14 Near-hole ($-5 \leq X/D \leq 0$) area-average of augmentation in cooling effectiveness
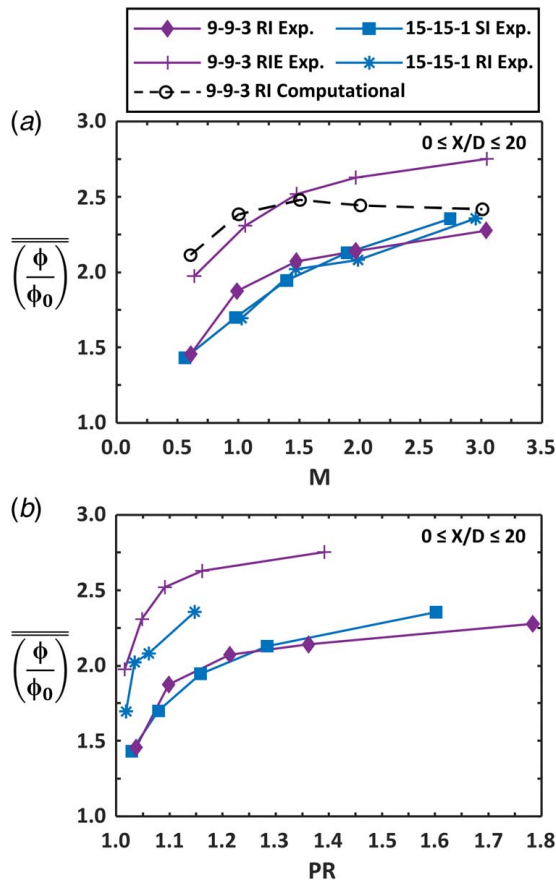
Fig. 15 Area-averaged augmentation in cooling effectiveness:
(a) across a range of blowing ratios for both as-built experimental
holes and the design intent computational holes and (b) across a
range of pressure ratios

Computational Results

Computational predictions of area-averaged ϕ/ϕ_0 for the 9-9-3 RI hole are presented in Fig. 15(a) along with comparisons to experimental results. Note that the computational predictions were based on the design geometry for the 9-9-3 RI hole, not the actual manufactured hole. As noted previously, the AM built holes had significant internal roughness that was not duplicated in the computational predictions. As is evident in Fig. 15(a), predicted area-averaged ϕ/ϕ_0 values for the 9-9-3 RI design intent hole were significantly higher than the experimentally measured values of the as-built hole, but quite similar to the values measured for the 9-9-3 RIE as-built hole. In a companion experimental study of the 9-9-3 RI and RIE holes built as designed [28], the performances of these two holes were found to be essentially the same. Consequently, the better performance of the 9-9-3 RIE in this study might be attributed this hole design being less susceptible to imperfections and roughness generated by the AM build at engine scale. And this sensitivity to imperfections may explain why the computational predictions had a better match to the RIE hole performance.

Useful insights in the cooling performance are obtained by examining midplane hole contours of local Ma and local non-dimensional temperature (θ) shown in Fig. 16 for $M = 2$ and 3. In both cases, it is evident from the local Mach number distribution that the flow separates at the downstream inlet of the hole even though a rounded inlet was used to reduce separation here. The local Mach number distributions also shows maximum local Mach numbers in the hole that were significantly higher than the mainstream Mach number of $Ma_\infty = 0.3$. For there was supersonic flow in the hole with a peak local Mach number of $Ma = 1.4$ just past the inlet. Careful inspection of the local Ma and θ contours in Fig. 16 reveals a shockwave that likely has a significant effect on the diffuser performance. As shown by the contours of θ for both $M = 2$ and $M = 3$, a significant increase in θ is predicted to occur, i.e. the coolant becomes much colder than the coolant temperature in the internal channel feeding the coolant hole. This decrease in coolant temperature is caused by the acceleration to high local Mach numbers that occurs in the hole. Note the higher
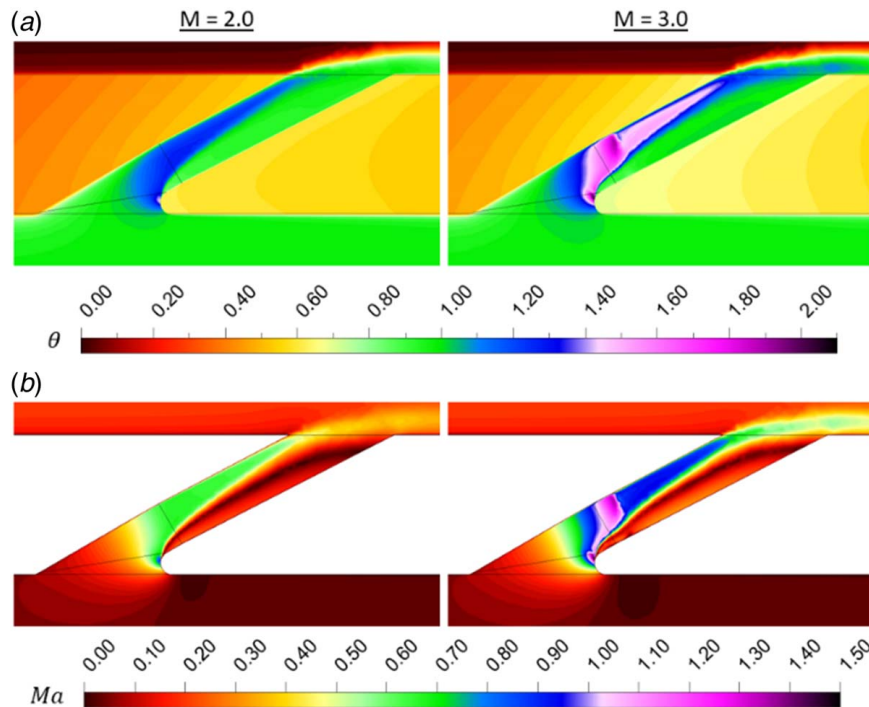

Fig. 16 Hole midplane contours of (a) θ and (b) Ma for the computational prediction at
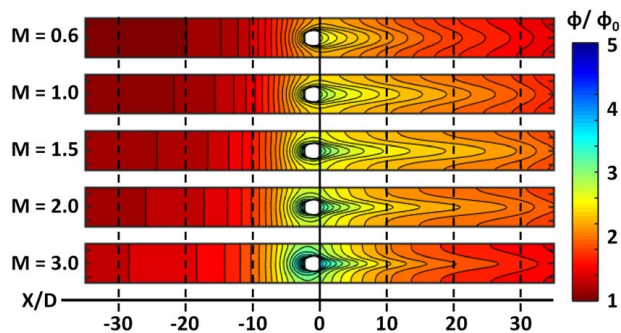$M = 2$ and $M = 3$ of the 9-9-3 RIE design intent

Fig. 17 Surface φ contours for the computational prediction across the range of _M_ studied for the design intent of the 9-9-3 RI hole

θ values in the solid around the as-designed hole show the effect of bore cooling.

The effects of bore cooling are also evident in the contours of f/f_0 upstream and downstream of the film cooling hole as shown in Fig. 17. As was noted previously in the discussion of the as-built holes, the cooling of the surface upstream of the hole is a good indication of the effect of bore cooling in the hole. The ϕ/ϕ_0 contours from the smooth 9-9-3 RI design intent hole show that there is significant cooling upstream of the hole, with noticeable cooling as much as 10D upstream of the hole for the $M = 3.0$ case. Note that the very strong bore cooling that occurs for $M > 2$ may be attributed to lower coolant temperatures and shock waves increasing turbulence in the hole. The increase in near-hole cooling with increasing M is consistent with the experimental results. The near-hole contours of the as-built 9-9-3 RI holes in Fig. 11(a) are similar to those of the computational results shown results in Fig. 17.

The area-averaged augmentation in cooling effectiveness of the as-designed 9-9-3 RI hole shown in Fig. 15(a) and the contours in Fig. 17 convey that the as-designed hole has an optimal operating point at $M = 1.5$, whereas the experimental holes continue to increase with increasing M. The discrepancy between the computational and experimental trends at the high blowing ratios is likely caused by the RANS model underpredicting the turbulent coolant dispersion.

Conclusions

The purpose of this study was to quantify, using four shaped holes, the ability to additively manufacture rounded inlets and exits. The four hole shapes studied were split into two diffuser angles groups: 9-9-3 and 15-15-1. Both 9-9-3 holes had inlet fillets, but at different radii, and one also had an exit fillet. One of the 15-15-1 holes had no fillets, and the other had an inlet fillet. Rows of five holes were printed in Inconel 718 test coupons using AM. Experiments were conducted at engine relevant conditions for the as-built film cooling holes.

X-ray computed tomography was used to characterize the as-built holes. Because the film cooling holes were printed in an orientation with the metering axis perpendicular to the substrate, the cross-sectional areas and hydraulic diameters of the cooling holes were slightly larger than the design intent. The holes with inlet fillets also contained inlet roughness features that occur because of the overhang distances during the build to create the leeward side of the hole.

Overall effectiveness measurements were made for engine relevant conditions using the four different hole shapes whereby the benefit was reported relative to no film-cooling. The near-hole augmentation in cooling effectiveness showed that the addition of an inlet fillet decreases the in-hole convection. However, all as-built geometries had similar near-hole effectiveness at high blowing ratios, indicating that the geometry has more of an effect on in-hole convection at low blowing ratios than it has at high blowing ratios.

For the effectiveness downstream of the holes, the inlet fillet was found to be a contributing factor to the decay in the augmentation of cooling effectiveness. The streamwise decay rates of the measured effectiveness values indicated that incorporating a rounded inlet into the hole design creates less film mixing than incorporating the sharp inlet. The hole with a rounded inlet and exit had the least decay, which signified that the exit fillet could significantly reduce the film mixing. As would be expected, the holes with a 15 deg expansion angle had better lateral spreading of the coolant thereby creating more uniform effectiveness across the span than holes with 9 deg lateral expansion. Results from a compressibility test showed that the cooling performance is independent of the external Mach number for $Ma_\infty < 0.47$ at low blowing ratios.

Computational predictions were also performed for the 9-9-3 RI hole, and comparisons were made to experimental results. The computational results overpredicted performance, acting similarly to RANS predictions in a previous study [16]. However, notable features of these predictions include in-hole behavior. At the highest blowing ratios, jet separation was predicted to be significant, and at $M = 3$ the formation of a normal shock in the hole was predicted. Rapid expansion of the coolant jet in turn reduces temperature in the hole and may augment bore cooling.

In all, this study showed that AM roughness features cause variations in inlet rounding, which impacts the overall effectiveness. Although, the as-built sharp inlet causes the highest in-hole convection, the sharp inlet causes more film mixing downstream than holes with fillets at the inlet or exit of the hole. Therefore, it is important for designers to understand how the as-built hole design impacts the cooling mechanisms which in turn impact the overall performance of AM film cooling holes.

Conflict of Interest

There are no conflicts of interest.

Data Availability Statement

The datasets generated and supporting the findings of this article are obtainable from the corresponding author upon reasonable request.

Nomenclature

h = convective heat transfer coefficient
k = thermal conductivity
ℓ = local cooling hole coordinate
p = perimeter

t = hole breakout width
D = film cooling hole metering diameter
H = channel height
L = cooling hole length
M = blowing ratio, $(\dot{m}_f/A_{min})/(\rho_\infty U_\infty)$
P = pressure or pitch hole spacing
T = temperature
U = maximum/centerline velocity
V = mass average velocity
X = streamwise distance
$\dot{m}$ = mass flowrate
t_{wall} = coupon wall thickness
A_c = cross-sectional flow area
A_{min} = minimum cross-sectional area of cooling hole meter
D_h = hydraulic diameter, $4A_c/p$
R_a = arithmetic mean roughness
AR = area ratio of hole exit to hole inlet
Bi = Biot number, $h_\infty t_{wall}/k_\infty$
DR = density ratio, ρ_c/ρ_∞
FP = mass flow parameter, $\dot{m}(RT_c)^{0.5}/P_c A_c$
Ma = Mach number
Nu = Nusselt number, hD_h/k
PR = pressure ratio
Re_{D_h} = Reynolds number, $V_i D_h/\nu$

Greek Symbols

θ = Non-dimensionalized temperature, $(T_\infty - T)/(T_\infty - T_c)$
ν = kinematic viscosity
ρ = fluid density
ϕ = overall effectiveness, $(T_\infty - T_s)/(T_\infty - T_c)$
$\bar{\phi}$ = laterally averaged overall effectiveness
$\bar{\bar{\phi}}$ = area-averaged overall effectiveness
$\bar{\bar{\phi}}_0$ = overall effectiveness without film cooling

Subscripts

c = coolant
d = downstream of cooling hole inlet
f = film
i = coupon internal channel
m = metering section
s = coupon surface
u = upstream of cooling hole inlet
DI = design intent
∞ = mainstream

References

[1] Snyder, J. C., and Thole, K. A., 2020, "Performance of Public Film Cooling Geometries Produced Through Additive Manufacturing," ASME J. Turbomach., **142**(5), p. 051009.
[2] Wildgoose, A. J., Thole, K. A., Sanders, P., and Wang, L., 2021, "Impact of Additive Manufacturing on Internal Cooling Channels With Varying Diameters and Build Directions," ASME J. Turbomach., **143**(7), p. 071003.
[3] Snyder, J. C., Stimpson, C. K., Thole, K. A., and Mongillo, D., 2016, "Build Direction Effects on Additively Manufactured Channels," ASME J. Turbomach., **138**(5), p. 051006.
[4] Wang, P., Sin, W. J., Nai, M. L. S., and Wei, J., 2017, "Effects of Processing Parameters on Surface Roughness of Additive Manufactured Ti-6Al-4V Via Electron Beam Melting," Materials, **10**(10), pp. 8–14.
[5] Wang, D., Yang, Y., Yi, Z., and Su, X., 2013, "Research on the Fabricating Quality Optimization of the Overhanging Surface in SLM Process," Int. J. Adv. Manuf. Technol., **65**(9–12), pp. 1471–1484.
[6] Snyder, J. C., and Thole, K. A., 2020, "Understanding Laser Powder Bed Fusion Surface Roughness," ASME J. Manuf. Sci. Eng., **142**(7), p. 071003.
[7] Snyder, J. C., Stimpson, C. K., Thole, K. A., and Mongillo, D. J., 2015, "Build Direction Effects on Microchannel Tolerance and Surface Roughness," ASME J. Mech. Des., **137**(11), p. 111411.
[8] Jones, F. B., Fox, D. W., Oliver, T., and Bogard, D. G., 2021, "Parametric Optimization of Film Cooling Hole Geometry," ASME Paper No. GT2021-59326.
[9] Goldstein, R. J., 1971, "Film Cooling," Adv. Heat Transf., **7**(C), pp. 321–379.
[10] Gritsch, M., Schulz, A., and Wittig, S., 1998, "Adiabatic Wall Effectiveness Measurements of Film-Cooling Holes With Expanded Exits," ASME J. Turbomach., **120**(3), pp. 549–556.
[11] Schroeder, R. P., and Thole, K. A., 2014, "Adiabatic Effectiveness Measurements for a Baseline Shaped Film Cooling Hole," ASME Paper No. GT2014-25992.
[12] Schroeder, R. P., and Thole, K. A., 2016, "Effect of High Freestream Turbulence on Flowfields of Shaped Film Cooling Holes," ASME J. Turbomach., **138**(9), p. 091001.
[13] Bryant, C. E., and Rutledge, J. L., 2020, "A Computational Technique to Evaluate the Relative Influence of Internal and External Cooling on Overall Effectiveness," ASME J. Turbomach., **142**(5), p. 051008.
[14] Schroeder, R. P., and Thole, K. A., 2017, "Effect of In-Hole Roughness on Film Cooling From a Shaped Hole," ASME J. Turbomach., **139**(3), p. 031004.
[15] Stimpson, C. K., Snyder, J. C., Thole, K. A., and Mongillo, D., 2018, "Effectiveness Measurements of Additively Manufactured Film Cooling Holes," ASME J. Turbomach., **140**(1), p. 011009.
[16] Jones, F. B., Fox, D. W., and Bogard, D. G., 2020, "Experimental and Computational Investigation of Shaped Film Cooling Holes Designed to Minimize Inlet Separation," ASME Paper No. GT2020-15561.
[17] McClintic, J. W., Fox, D. W., Jones, F. B., Bogard, D. G., Dyson, T. E., and Webster, Z. D., 2019, "Flow Physics of Diffused-Exit Film Cooling Holes Fed by Internal Crossflow," ASME J. Turbomach., **141**(3), p. 031010.
[18] Kohli, A., and Thole, K. A., 1998, "Entrance Effects on Diffused Film-Cooling Holes," ASME Paper No. 88-GT-402.
[19] Fraas, M., Glasenapp, T., Schulz, A., and Bauer, H. J., 2019, "Optimized Inlet Geometry of a Laidback Fan-Shaped Film Cooling Hole—Experimental Study of Film Cooling Performance," Int. J. Heat Mass Transf., **128**, pp. 980–990.
[20] Hay, N., Lampard, D., and Khaldi, A., 1994, "Coefficient of Discharge of 30° Inclined Film Cooling Holes With Rounded Entries or Exits," ASME Paper No. 94-GT-180.
[21] Stimpson, C. K., Snyder, J. C., Thole, K. A., and Mongillo, D., 2017, "Scaling Roughness Effects on Pressure Loss and Heat Transfer of Additively Manufactured Channels," ASME J. Turbomach., **139**(2), p. 021003.
[22] Electro Optical Systems, 2020, EOS NickelAlloy IN718 Material Data Sheet.
[23] Reinhart, 2011, "Industrial CT & Precision," Application of CT Scanning in Industry, Heidelberg, Germany.
[24] Kays, W. M., Crawford, M. E., and Weigand, B., 2004, Convective Heat & Mass Transfer, McGraw-Hill, Inc., Boston, MA, pp. 260–271.
[25] Figliola, R., and Beasley, D., 1995, Theory and Design for Mechanical Measurements, John Wiley & Sons, Hoboken, NJ, pp. 171–209.
[26] Zhou, W., Johnson, B., and Hu, H., 2017, "Effects of Flow Compressibility and Density Ratio on Film Cooling Performance," J. Propuls. Power, **33**(4), pp. 964–974.
[27] Harrison, K. L., and Bogard, D. G., 2008, "Comparison of RANS Turbulence Models for Prediction of Film Cooling Performance," ASME Paper No. GT2008-51423.
[28] Furgeson, M. T., Veley, E. M., Yoon, C., Gutierrez, D., Bogard, D. G., and Thole, K. A., "Development and Evaluation of Shaped Film Cooling Holes Designed for Additive Manufacturing", ASME Paper No. GT2022-83201.